

# Non-WKB Models of the FIP Effect: The Role of Slow Mode Waves

J. Martin Laming

*Space Science Division, Naval Research Laboratory Code 7674L, Washington, D.C. 20375*

## ABSTRACT

A model for element abundance fractionation between the solar chromosphere and corona is further developed. The ponderomotive force due to Alfvén waves propagating through, or reflecting from the chromosphere in solar conditions generally accelerates chromospheric ions, but not neutrals, into the corona. This gives rise to what has become known as the First Ionization Potential (FIP) Effect. We incorporate new physical processes into the model. The chromospheric ionization balance is improved, and the effect of different approximations is discussed. We also treat the parametric generation of slow mode waves by the parallel propagating Alfvén waves. This is also an effect of the ponderomotive force, arising from the periodic variation of the magnetic pressure driving an acoustic mode, which adds to the background longitudinal pressure. This can have subtle effects on the fractionation, rendering it quasi-mass independent in the lower regions of the chromosphere. We also briefly discuss the change in the fractionation with Alfvén wave frequency, relative to the frequency of the overlying coronal loop resonance.

*Subject headings:* Sun:abundances – Sun:chromosphere – turbulence – waves

## 1. Introduction

The First Ionization Potential (FIP) effect is the by now well known enhancement in abundance by a factor of 3-4 over photospheric values of elements in the solar corona with FIP less than about 10 eV. These low FIP elements include Fe, Si, Mg, etc. Elements with FIP greater than 10 eV (high-FIP) mostly retain their photospheric composition. This was actually first observed in the 1960's (Pottasch 1963), making it nearly as old as the problem of coronal heating. It has been taken seriously as a phenomenon since the mid 1980's (Meyer 1985ab). There are a number of studies of the FIP effect in different regions of the solar corona and wind, reviewed in Feldman & Laming (2000) and Laming (2004),

and references therein. With the launch of the Extreme Ultraviolet Explorer (EUVE) in the 1990’s, it became clear that element abundances in late-type stellar coronae also do not always resemble the stellar photospheric composition. The FIP effect is also observed in many solar-like late type stars. At higher activity levels and/or later spectral types, a so called “inverse FIP” effect is observed, where the low FIP elements are depleted in the corona (e.g. Wood & Linsky 2010).

A variety of models have been proposed to explain these phenomena. Laming (2004, 2009) review many of these different scenarios, and argue that the ponderomotive force is the most likely agent of FIP fractionation. This force arises as Alfvén waves propagate through the chromosphere, and acts on chromospheric ions, but not neutrals. Physically, it corresponds to the interaction of waves and plasma through the refractive index of the medium. Waves carrying significant energy and momentum refracting or reflecting in a plasma must exert a force, in this case on the charged particles that contribute to the dielectric tensor, but not on the neutrals. The ponderomotive force in the chromosphere may in principle be directed upwards or downwards, giving rise to FIP or so-called “inverse FIP” effects respectively (i.e. a coronal enhancement or depletion of low FIP ions).

The chromosphere-corona interface is generally a barrier to Alfvén wave propagation; upcoming waves from the chromosphere are usually reflected back down again, and downward directed waves from the corona reflect back upwards, as illustrated in the right hand footpoint (chromosphere B) in Figure 1. Alfvén waves with predominantly coronal origin generally give rise to the positive (i.e. solar-like) FIP effect, while waves generated by upward propagating acoustic waves associated with stellar convection may produce inverse FIP effect. The association of coronal abundance anomalies with Alfvén waves gives us a unique and unexpected diagnostic with which to explore the behavior of MHD turbulence in solar and stellar upper atmospheres. While we will argue that the coronal Alfvén waves themselves are actually byproducts of processes that heat solar and stellar coronae, (most likely accomplished by various forms of “nanoflares”), an understanding of coronal abundance anomalies still becomes far more central to exploring coronal heating than would be the case in prior models for the fractionation invoking thermal processes such as diffusion.

In this paper we seek to develop the ponderomotive force model incorporating the parametric generation of parallel propagating slow mode waves by the Alfvén waves themselves, together with revisions to some of the atomic data. First, in section 2, we review the important features of the Laming (2004, 2009) model. Section 3 outlines the various theoretical refinements made in this paper, and section 4 describes new results for fractionations in open and closed magnetic field configurations. Section 5 discusses in more detail the effect of the parametric generation of slow mode waves and its implications for fractionation in closed

coronal loops and in the slow speed solar wind. We also consider limits on the upward flow speed through the chromosphere, and make final conclusions.

## 2. The Ponderomotive Model Revisited

The ponderomotive force stems from second order terms in  $\delta\mathbf{J} \times \delta\mathbf{B}/c$  and  $\rho\delta\mathbf{v} \cdot \nabla\delta\mathbf{v}$  in the MHD momentum equation. It can be manipulated (e.g Litwin & Rosner 1998, Laming 2009) for waves of frequency  $\omega_A \ll \Omega$ , the ion gyrofrequency, into the time averaged form

$$F = \frac{\partial}{\partial z} \left( \frac{q^2 \delta E_{\perp}^2}{4m\Omega^2} \right) = \frac{mc^2}{4} \frac{\partial}{\partial z} \left( \frac{\delta E_{\perp}^2}{B^2} \right), \quad (1)$$

where  $\delta E_{\perp}$  is the perpendicular wave electric field and  $q$  is the ion charge. The ponderomotive acceleration,  $F/m$ , is independent of the ion mass. The Laming (2004, 2009) model comes about as a natural extension of existing work on Alfvén wave propagation in the solar atmosphere with essentially no extra physics required. It is also the model most worked out in detail to interpret observations, giving it unique potential for diagnosing wave processes in the corona and chromosphere.

The basic model builds on Hollweg (1984), where upward propagating Alfvén waves were introduced at one loop footpoint. Here they could reflect back down into the chromosphere, or be transmitted into the loop, where they propagated back and forth with a small probability of leaking back into the chromosphere at each end. With reference to Figure 1, we initiate our simulations with one downward propagating wave at the  $\beta \sim 1.2$  layer in chromosphere A, and integrate the Alfvén wave transport equations (see below) to chromosphere B to evaluate the standing wave pattern there. The chromosphere at each footpoint can be based on any of the Vernazza, Avrett, & Loeser (1981) models or similar. Here we use the Avrett & Loeser (2008) update of VALC. The ionization balance of the minor ions is computed at each height in the chromosphere using the model temperature and electron density, and a coronal UV-X-ray spectrum appropriately absorbed in the intervening chromospheric layers. We have tried a number of different spectra based on Vernazza & Reeves (1978), or model flare spectra computed using CHIANTI (see e.g. Huba et al. 2005, for the 2000 Bastille Day flare). The atomic data are as in Laming (2004) and Laming (2009), with estimates for the charge exchange ionization for Si, Fe, and other low FIP elements added (see subsection 3.3). The chromospheric magnetic field is taken to be a 2D force free field from Athay (1981) and designed to match chromospheric magnetic fields in Gary (2001) and Campos & Mendes (1995), which represents the expansion of the field from the high  $\beta$  photosphere where the field is concentrated into small network segments, into the low  $\beta$  chromosphere where the field expands to fill much more of the volume.

We model the Alfvén waves in a non-WKB approximation. The procedure follows that described in detail by Cranmer & van Ballegoijen (2005), but applied to closed rather than open magnetic field structures. The curvature of the loop is neglected. For Alfvén waves, where the energy flux is necessarily directed along the field direction, this is unlikely to have a significant effect. Some extra damping may result as the wave develops a component of its wavevector perpendicular to the field, but we neglect this and all other damping mechanisms in this work. The transport equations are

$$\frac{\partial z_{\pm}}{\partial t} + (u \pm V_A) \frac{\partial z_{\pm}}{\partial r} = (u \pm V_A) \left( \frac{z_{\pm}}{4H_D} + \frac{z_{\mp}}{2H_A} \right), \quad (2)$$

where  $z_{\pm} = \delta v_{\perp} \pm \delta B_{\perp} / \sqrt{4\pi\rho}$  are the Elsässer variables for Alfvén waves propagating against or along the magnetic field respectively, and are valid for torsional or planar Alfvén waves. The Alfvén speed is  $V_A$ , the upward flow speed is  $u$  and the density is  $\rho$ . The signed scale heights are  $H_D = \rho / (\partial\rho/\partial r)$  and  $H_A = V_A / (\partial V_A/\partial r)$ . In the solar chromosphere and corona  $u \ll V_A$ , and we put  $u = 0$ . The calculation of  $V_A$  uses the total (ionized and neutral) gas density, since the wave frequencies of interest here are well below the charge exchange rate, and neutrals are well coupled to the wave. Charge changing collisions involving electrons (impact ionization, and radiative and dielectronic recombination) are generally slower than charge exchange in chromospheric conditions. Hence in considering the wave propagation, ion-neutral friction is neglected, though it is included in the evaluation of the fractionation.

The fractionations are calculated by postprocessing the non-WKB wave. This is valid because the fractionation has a negligible effect on the wave propagation. The degree of fractionation is given by the formula

$$\text{fractionation} = \exp \left( 2 \int_{z_l}^{z_u} \xi_s a \nu_{eff} / \nu_{s,i} / v_s^2 dz \right) \quad (3)$$

(see equation 9, Laming 2009, equation 12, Laming 2004, which follow Schwadron et al. 1999), where  $\xi_s$  is the ionization fraction of element  $s$ ,  $a$  is the ponderomotive acceleration,  $\nu_{eff} = \nu_{s,i} \nu_{s,n} / [\xi_s \nu_{s,n} + (1 - \xi_s) \nu_{s,i}]$  where  $\nu_{s,i}$  and  $\nu_{s,n}$  are the collision rates of ions and neutrals, respectively, of element  $s$  with the ambient gas. Also  $v_s^2 = kT/m_s + v_{\mu turb}^2 + v_{turb}^2$ , where  $v_{\mu turb}$  is the amplitude of microturbulence coming from the Avrett & Loeser (2008) chromospheric model, and  $v_{turb}$ , discussed further in section 3.2, is the amplitude of longitudinal waves induced by the Alfvén waves themselves. The limits of integration,  $z_l$  and  $z_u$  are the lower and upper limits over which the ponderomotive force acts. We take  $z_l$  to be where  $\beta \simeq 1$ , and  $z_u$  is in the transition region at an altitude where all elements are ionized.

### 3. New Model Features

#### 3.1. Slow Mode Waves

We have introduced an extra longitudinal pressure associated with the Alfvén waves proportional to  $v_{turb}^2$ , which has the effect of causing some saturation of the FIP fractionation. Here we give the physical motivation for this extra term, which arises from the generation of slow mode waves. Physically, the periodic variation in magnetic pressure of the Alfvén wave drives longitudinal compressional waves. These generated acoustic waves can act back on the Alfvén driver, as the compressional wave introduces a periodic variation in the Alfvén speed, which generates new Alfvén waves. We illustrate the generation of slow mode or acoustic waves by the ponderomotive force associated with plane Alfvén waves with a simple 1D calculation. The linearized momentum equation keeping terms to all orders in perturbed quantities is (all symbols have their usual meanings),

$$(\rho + \delta\rho) \frac{\partial \delta v_z}{\partial t} + (\rho + \delta\rho) \delta v_z \frac{\partial \delta v_z}{\partial z} = (\rho + \delta\rho) \frac{\partial}{\partial z} \frac{\delta B^2}{8\pi(\rho + \delta\rho)} - \frac{\partial \delta P}{\partial z} - g\delta\rho, \quad (4)$$

where

$$\begin{aligned} \delta\rho &= -\rho \nabla \cdot \xi - \xi_z \frac{\partial \rho}{\partial z} = -\rho \xi \left( ik_s + \frac{1}{L_\rho} \right) \\ \delta P &= -\gamma P \nabla \cdot \xi - \xi_z \frac{\partial P}{\partial z} = -P \xi \left( ik_s \gamma + \frac{1}{L_P} \right) \end{aligned} \quad (5)$$

for Eulerian displacement  $\xi \propto \exp i(\omega_s t + k_s z)$ , where  $L_P = P/(\partial P/\partial z)$  and  $L_\rho = \rho/(\partial \rho/\partial z)$  (signed) pressure and density scale heights respectively. The first term on the right hand side of equation 4 represents the instantaneous ponderomotive force. In cases where the WKB approximation applies,  $\delta B \propto \rho^{1/4}$ , and this expression is equivalent to the more usual form  $-\partial(\delta B^2/8\pi)/\partial z$ . Substituting for  $\delta\rho$  and  $\delta P$  from equations 5, keeping terms as high as second order in small quantities, equation 3 becomes

$$-i \frac{\omega_s}{L_\rho} \delta v_z^2 + \left( -\omega_s^2 + k_s^2 c_s^2 - i \frac{k_s c_s^2}{L_P} - \frac{c_s^2}{\gamma L_P^2} - i \frac{k_s c_s^2}{\gamma L_P} - ik_s g - \frac{g}{L_\rho} \right) \delta v_z - i \omega_s \frac{\partial}{\partial z} \frac{\delta B^2}{8\pi\rho} = 0. \quad (6)$$

This is considerably simplified in isothermal conditions,  $\gamma = 1$ ,  $L_P = L_\rho = -c_s^2/g$ , so that

$$-i \frac{\omega_s}{L_\rho} \delta v_z^2 + (-\omega_s^2 + k_s^2 c_s^2 + ik_s g) \delta v_z - i \omega_s \frac{\partial}{\partial z} \frac{\delta B^2}{8\pi\rho} = 0. \quad (7)$$

We put  $\Im k_s = -g/2c_s^2$ , and  $\sqrt{(\Re k_s)^2 + g^2/4c_s^4} = 2\Re k_A/n$ ,  $\omega = 2\omega_A/n$ , where  $k_A$  and  $\omega_A$  are the wavevector and angular frequency of the Alfvén wave with  $n = 1, 2, 3, \dots$  (anticipating the result below). We find

$$\delta v_z^2 - \delta v_z i L_\rho \omega_s \left( 1 - \frac{c_s^2}{V_A^2} \right) + L_\rho \frac{\partial}{\partial z} \frac{\delta B^2}{8\pi\rho} = 0 \quad (8)$$

with solution

$$\delta v_z = \frac{-i}{2} \left[ \sqrt{\delta v_A^2 + L_\rho^2 \omega_s^2 \left(1 - \frac{c_s^2}{V_A^2}\right)^2} - L_\rho \omega_s \left(1 - \frac{c_s^2}{V_A^2}\right) \right] \quad (9)$$

where we have put  $\frac{\partial}{\partial z} (\delta B^2/8\pi\rho) = (\delta B^2/4\pi\rho)/4L_\rho = \delta v_A^2/4L_\rho$  using the WKB result for Alfvén waves in a density gradient, and assuming  $1/L_\rho \gg \Re k_A$ . When  $c_s^2 \sim V_A^2$  or  $L_\rho \rightarrow 0$ ,  $\delta v_z \simeq -i\delta v_A/2$ . In the opposite limit  $\delta v_z \simeq -i\delta v_A^2/4L_\rho\omega_s(1 - c_s^2/V_A^2)$ . In these two cases  $\omega_s = \omega_A$  or  $\omega_s = 2\omega_A$  respectively. In fact acoustic waves can be generated with  $\omega_s = 2\omega_A/n$ , with higher  $n$  becoming more intense as the nonlinearity increases (Landau & Lifshitz 1976). Vasheghani Farahani et al. (2011) treat the case of slow mode wave generation by a torsional Alfvén wave. This is subtly different to the case of a plane Alfvén wave considered here, and the FIP fractionation resulting from such a model will be investigated in a future paper.

Anticipating applications to possibly nonlinear Alfvén and slow mode wave amplitudes, we revisit the analysis above retaining more higher order terms. From  $\delta\rho = -\rho\xi(k_s + 1/L)$  we derive

$$\frac{\partial\delta\rho}{\partial z} = \delta\rho \left(ik_s + \frac{1}{L}\right). \quad (10)$$

which when substituted into the linearized continuity equation,

$$\frac{\partial\delta\rho}{\partial t} + \frac{\partial}{\partial z} (\rho\delta v_z + \delta\rho\delta v_z) = 0, \quad (11)$$

with the time derivatives  $\partial\delta v_z/\partial t = i\omega_s\delta v_z$  and  $\partial\delta\rho/\partial t = i\omega_s\delta\rho$ , gives

$$\delta\rho = -(ik_s + 1/L_\rho) \frac{\rho\delta v_z}{i\omega_s} \left(1 + \frac{2k_s\delta v_z}{\omega} + \frac{\delta v_z}{i\omega L_\rho}\right)^{-1}. \quad (12)$$

Writing  $\delta P = \gamma P (\delta\rho/\rho + \delta v_z/i\omega L_\rho) - P\delta v_z/i\omega L_P$  we similarly derive

$$\frac{\partial\delta P}{\partial z} = \left(\frac{1}{L_P} + ik_s\right) \left(c_s^2\delta\rho + P\frac{\delta v_z}{i\omega} \left(\frac{\gamma}{L_\rho} - \frac{1}{L_P}\right)\right). \quad (13)$$

We now eliminate  $\delta\rho$  and  $\delta P$  in favor of  $\delta v_z$  in equation 3 to derive a quartic equation in  $\delta v_z$  for the driven slow mode wave with angular frequency  $\omega_s$  and wavevector  $k_s$ ;

$$\begin{aligned} & \delta v_z^4 \left[ -\frac{k_s^3}{\omega_s} \right] + \delta v_z^3 \left[ -3k_s^2 + \left( \frac{c_s^2}{L_\rho} - \frac{c_s^2}{\gamma L_P} \right) \left( \frac{1}{L_P} + ik_s \right) \left( \frac{2k_s^2}{\omega_s^2} + \frac{k_s}{i\omega_s^2 L_\rho} \right) \right] \\ + & \delta v_z^2 \left[ -3k_s\omega_s + \left( \frac{c_s^2}{L_\rho} - \frac{c_s^2}{\gamma L_P} \right) \left( \frac{1}{L_P} + ik_s \right) \left( \frac{2k_s}{\omega_s} + \frac{1}{i\omega_s L_\rho} \right) + \frac{k_s^3 c_s^2}{\omega_s} - i\frac{k_s^2 c_s^2}{\omega_s L_P} - \frac{k_s c_s^2}{\gamma\omega L_P^2} \right] \\ + & \delta v_z^2 \left[ -i\frac{k_s^2 c_s^2}{\gamma\omega_s L_P} - i\frac{k_s^2 g}{\omega_s} - \frac{gk_s}{\omega_s L_\rho} + \left( 2ik_s + \frac{1}{L_\rho} \right) \left( ik_A \delta v_A^2 \frac{k_s}{\omega_s} + \frac{\delta v_A^2 k_s}{2\omega L_\rho} + \frac{\delta v_A^2 ik_s^2}{2\omega_s} \right) \right] \\ + & \delta v_z \left[ -\omega_s^2 + k_s^2 c_s^2 - i\frac{k_s c_s^2}{L_P} - \frac{c_s^2}{\gamma L_P^2} - ik_s \frac{c_s^2}{\gamma L_P} - ik_s g - \frac{g}{L_\rho} + \left( 3ik_s + \frac{1}{L_\rho} \right) ik_A \delta v_A^2 + \frac{i\delta v_A^2 k_s}{2L_\rho} - \frac{\delta v_A^2 k_s^2}{2} \right] \end{aligned}$$

$$-\omega_s k_A \delta v_A^2 = 0. \quad (14)$$

To lowest order, the terms in  $\delta v_z$  and the constant are the same as in equation 6. The quadratic and higher terms are changed, because of the difference between equations 12 and 13, and those in equation 5. Inserting even accurate spatial derivatives in place of those in equations 12 and 13 would generate yet more higher order terms, extending  $n$  in principle without limit. Landau & Lifshitz (1976) give a similar conclusion in their treatment of parametric resonance.

We solve equation 14 numerically, with the same  $k_s$  (real and imaginary parts) as above. We select the solution with the lowest absolute magnitude as the physically correct solution for our problem, this being the solution that goes to zero as  $\delta v_A \rightarrow 0$ . This is always close to the solution obtained discarding all terms of order higher than  $\delta v_z^2$  in equation 14, and usually close to the case when the term in  $\delta v_z^2$  is also neglected. This describes turbulence for parallel propagating waves. Zaqarashvili & Roberts (2006) give a detailed treatment of the interaction between weak Alfvén and sound waves in a homogeneous medium, where acoustic and Alfvén speeds are equal. The stronger generation of acoustic waves by the ponderomotive force in a density gradient is demonstrated by the simulations of Del Zanna et al. (2005), where slow mode waves are seen propagating up from loop footpoints with properties consistent with the solutions of equations 9 or 14.

Closer to the layer where  $c_s^2 = V_A^2$ , the magnetic field becomes more curved, giving rise to higher perpendicular components of Alfvén wave wavevectors, and potentially stronger turbulent cascade and/or mode conversion. In this case we expect stronger slow mode waves. In Laming (2009) we assumed  $\delta v_s = \delta v_A$ . However considerations of mode conversion for initially upward propagating acoustic waves suggest that higher slow mode intensities than this should be present. Khomenko & Cally (2011) report that at conditions for maximum conversion of a high  $\beta$  fast mode wave to a low  $\beta$  Alfvén wave, the low  $\beta$  slow mode wave has 2-3 times more flux. In this paper, we make the approximation

$$\delta v_s^2 = \delta v_z^2 + 6\delta v_A^2 c_s^2 / V_A^2, \quad (15)$$

where  $\delta v_z$  represents the solution of equation 14, and the factor 6 in the last term is motivated by calculations illustrated in Cranmer et al. (2007) and Khomenko (2010). Slow mode waves governed by equation 15 have the effect of suppressing fractionation in the low chromosphere close to where the plasma  $\beta \simeq 1.2$ . Studies of mode conversion between acoustic and Alfvén waves generally show the upward moving acoustic wave beginning to convert to Alfvén waves at the  $\beta \simeq 1.2$  layer, and mode conversion continuing over a range of altitudes of order 100's of km (e.g Cally & Goossens 2008). The explicit incorporation of such effects is well beyond the scope of the work here, and the prescription in equation 15 should be sufficient to avoid

the occurrence of unphysical fractionations. Even so, it remains a feature of this work requiring further investigation in future papers.

### 3.2. Normalization Relative to Oxygen

In previous papers Laming (2004, 2009) we have discussed FIP fractionations relative to H. However the derivation of 3 has assumed fractionated elements are minor species, with the fractionation having no back reaction on the flow due to the neglect of inertial terms. Thus it is more appropriate to present and describe element fractionations with respect to another minor element. We choose O, which is a common choice for observers also.

### 3.3. Charge Exchange Ionization

Charge exchange rates have been previously taken from the compilation of Kingdon & Ferland (1996). These have been supplemented more recently with charge exchange ionization rates for Si and Fe, colliding with protons. We implement an estimate of the charge exchange ionization rate for all ions with lower FIP than H as follows. We estimate the radius  $R$  at which the sum of the binding energy of the electron in the target neutral and the polarization potential energy of the target neutral in the electric field of the incoming proton and equal to the equivalent sum for the resulting neutral H atom in the electric field of the newly formed ion, (known as the radius of the potential crossing) from

$$V = -\frac{(\alpha_s - \alpha_H)}{R^4} = -I_H + I_s \quad (16)$$

where  $V$  represents the difference in potential energy of the proton in terms of the polarizability  $\alpha_s$  of the target atom and resulting ion in terms of  $\alpha_H$ , the polarizability of the resulting hydrogen atom.  $I_H$  and  $I_s$  are the ionization potentials of hydrogen and the target atom,  $s$ , respectively. Polarizabilities and ionization potential here are in atomic units. The cross section is then  $\sigma_{cxi} = \pi R^2/2 = \pi \sqrt{(\alpha_s - \alpha_H) / (I_H - I_s)} / 2$ , assuming the maximum probability for a reaction is  $1/2$ . This estimate is a slightly different form of the Langevin formula given by Ferland et al. (1997). This approximation gives good agreement with the calculations of Allan et al. (1988) for charge exchange ionization of Mg. These authors comments that similar rates should exist for all other elements with ionization potentials below that of H, and we apply it to all of these elements. The charge exchange implemented is just the thermal process. No account is taken of any possible effects of the waves on the chromospheric ionization balance.



### 3.4. Comparison of Different Approximations

Carlsson & Stein (2002) have argued that the concept of an “average” chromosphere pursued by Avrett & Loeser (2008) and its antecedents is invalid, due to the extreme dynamics associated with chromospheric shock waves, arguing that “the mean value of a dynamic property is not the same as that property evaluated for the mean atmosphere”. Avrett & Loeser (2008) derive mean values for plasma properties based on observations, not on calculated mean atmospheres. More importantly, Carlsson & Stein (2002) show that the ionization fraction for H varies very little about its mean, due to the length of ionization and recombination times compared to the frequencies of shocks, and that their average electron density agrees very well with that in the Vernazza, Avrett, & Loeser (1981) model C. It is easy to see that other high FIP elements should behave similarly, and that the ionization balance we calculate (the overwhelmingly most important chromospheric property to us) should not be greatly in error, if at all. The inclusion of charge exchange ionization (section 3.3) increases the ionization level for all other elements as the ionization of hydrogen is increased above its thermal equilibrium level. The  $\text{Ca}^+$  to  $\text{Ca}^{2+}$  ionization balance is considered by Wedemeyer-Böhm & Carlsson (2011). This is more variable than that for H to  $\text{H}^+$  in Carlsson & Stein (2002), but is less of a concern to us, since the ponderomotive force experienced by an ion is independent of ion charge, so long as  $\omega_A \ll \Omega$ .

We give sample calculations that go some way to quantifying the effect of these issues. Figure 2 shows the coronal section of the 100,000 km long loop with magnetic field  $B = 20\text{G}$ . The density at the loop apex is  $5 \times 10^8 \text{ cm}^{-3}$ . This gives a resonant angular frequency of  $0.07 \text{ rad s}^{-1}$ . A wave of this frequency propagates on the loop, which is thus half a wavelength long. The top panel gives the Elsässer variables (real and imaginary parts), the middle panel gives the wave energy fluxes and their difference, and the third panel gives the ponderomotive acceleration. Figure 3 shows the chromospheric section of the loop where the fractionations are evaluated. This has the same three panels as for Figure 2, where the third panel also gives the slow mode wave amplitude, with a fourth panel (bottom right) that gives FIP fractionation and the ionization fraction of elements Fe, Mg, S, and He relative to O. In Table 1 fractionations for He, C, N, Ne, Mg, Si, S, Ar, and Fe relative to O are displayed, calculated according to our basic model described above, labeled “baseline”. In the succeeding columns, we give FIP fractionations calculated with different modifications to the model. In the first case the density given by Avrett & Loeser (2008) is modified so that the model density is consistent with the H ionization fraction and the assumption of photoionization-recombination equilibrium. The second variation gives fractionations calculated assuming the ionization fractions to be given by the Saha equation at the temperature and density in the chromospheric model. The first variation reduces the degree of ionization in the chromosphere, while the second one increases it. This has the

opposite effect on the fractionations, since these are given relative to O, and the increase or decrease of the ionization of O has a bigger effect on its fractionation than is the case with the other elements. As can be seen, the basic phenomenon of the FIP effect remains unaffected by the choice of approximation, but some of the details, e.g. the Mg/Fe ratio are subtly different. We return to discuss this in more detail below, in subsection 4.2.

The final column in Table 1 gives the FIP fractionation calculated with the assumption of slow mode wave amplitude  $\delta v_z = \delta v_A$ , the amplitude of the Alfvén wave, as taken in Laming (2009), instead of implementing the solution of equation 14. The overall fractionation is reduced for the same Alfvén wave amplitude, due to the increase in longitudinal pressure with the higher slow mode wave amplitude. In Laming (2009), we found that the FIP Effect saturated in this case at values around 3-4 for arbitrarily high Alfvén wave amplitude. In section 4, we will consider the behavior of the FIP Effect with resonant and nonresonant waves.

## 4. Results

### 4.1. Coronal Hole

A coronal hole is modeled in the same fashion. The chromosphere is identical to the case above, and the density evolves smoothly off-limb, declining to about  $2 \times 10^6 \text{ cm}^{-3}$  at an altitude of  $5 \times 10^5 \text{ km}$  (as in e.g. Figure 5 of Cranmer 2009). The magnetic field follows the model of Banaskiewicz et al. (1998). We take the coronal hole Alfvén wave spectrum calculated by Cranmer et al. (2007) as our starting point. It is illustrated in their Figure 3 for a position in the solar transition region. It is represented by the five wave frequencies and amplitudes at the starting position of the non-WKB integration of the wave transport equations, in this case at an altitude of 500,000 km. Parameters are chosen to match Figure 9 in Cranmer et al. (2007), and are given in Table 2 as the spectrum labeled “v0”. Figure 4 shows the wave amplitudes in the coronal hole section of the calculation, with the same three panels as for Figure 2, but illustrated up to an altitude of 500,000 km. Figure 5 shows the chromospheric response with the same four panels as in Figure 3. The ponderomotive acceleration (Figure 5, top right) has a similar “spike” at the top of the chromosphere as in Figure 3 for the closed loop, but is about an order of magnitude weaker. Lower down, the Alfvén wave amplitudes, and the corresponding slow mode wave amplitudes are larger than before. The net effect of smaller ponderomotive acceleration and higher slow mode wave amplitude is to reduce the FIP effect from the case in Figure 3. The resulting fractionation here is very similar to that found by Cranmer et al. (2007). In models v1-2 in Table 2, we increase the amplitude of the highest and lowest frequency wave in the spectrum respectively.

Increasing the highest frequency wave amplitude has the effect of increasing the fractionation predicted, while increasing the low frequency wave has very little effect. The results from all three models are summarized in Table 3, and compared with observations for various open field regions. Reasonable agreement for the fractionation of low FIP elements is seen. A small depletion of He is seen, but not as large as observed. Our purpose here has not been to provide a definitive calculation of the FIP effect in a coronal hole, but merely to illustrate that the observed difference between the FIP effect in closed and open field lines arises naturally in this model.

## 4.2. Closed Loop

We now explore fractionation in a closed coronal loop, illustrating the difference that a coronal resonant frequency can make to the fractionation. In Table 4 we give the fractionations computed for a closed loop with length 100,000 km, and a magnetic field of 20 G. A coronal wave at the loop resonant angular frequency of  $0.07 \text{ rad s}^{-1}$  is modeled. The wave transport equations (equation 2) are integrated from the  $\beta = 1$  layer in one chromosphere, where and initially downgoing wave amplitude is specified, through the loop to the opposite chromospheric footpoint, where the FIP fractionations are evaluated. The initial wave amplitudes are 0.4, 0.5, and  $0.6 \text{ km s}^{-1}$ , giving coronal wave peak amplitudes of approximately 55, 70, and  $82 \text{ km s}^{-1}$  respectively.

These cases illustrate the variation of the FIP effect with wave amplitude. The six columns on the right hand side give various observations of FIP fractionation. Zurbuchen et al. (2002) and von Steiger et al. (2000) both give fractionations measured *in situ* in the solar wind over relatively long periods of time. Giammanco et al. (2007, 2008) give fractionations also measured in the solar wind, but over time periods selected such that the wind speed was close to 380, 390 or  $400 \text{ km s}^{-1}$ . Phillips et al. (2003); Sylwester et al. (2010a,b); McKenzie & Feldman (1994) give abundance ratios measured spectroscopically in solar flares, and Bryans et al. (2009) observe quiet solar corona above the western limb, also spectroscopically. While the agreement between the FIP fractionations calculated for the initial Alfvén wave amplitude corresponding to  $0.5 \text{ km s}^{-1}$  is generally good, there are some important discrepancies. The ratio C/O is typically observed in the solar wind to be higher than calculated, as is S/O for some of the observations. While Fe/O and Mg/O are reasonably well reproduced, the direct ratio between Fe and Mg is not, except in the case of Bryans et al. (2009). The last case, with initial wave amplitude  $0.6 \text{ km s}^{-1}$ , is designed to match these observations, and does quite well. Only K is seriously discrepant, with S also somewhat underestimated. In the solar wind and flare observations, Fe and Mg are often

fractionated by the same amount.

Table 5 gives FIP fractionations for varying Alfvén wave frequency, with the amplitudes chosen to keep the Fe/O abundance ratio close to 4 as is often observed. Here, we have also included a wave field of chromospheric origin designed to have the same properties as that in the v0 model for the open field case. Downgoing wave amplitudes are specified at the  $\beta = 1$  layer in one chromosphere, and then the wave transport equations are integrated back to the opposite footpoint where FIP fractionations are evaluated. The column corresponding to the resonant frequency of  $0.07 \text{ rad s}^{-1}$  is the same as in Table 4, but for the new model. The chromospheric waves can be seen to have rather little effect, with the biggest changes being seen in the increased fractionations of C/O and S/O. Moving away from this resonance, either to lower or higher frequency, the C/O and S/O ratios increase to better agree with observations. At higher frequency so too does the Mg/O ratio, so that Mg and Fe fractionate more closely to the same degree; quasi-mass independent fractionation is achieved. Going to yet higher frequency, all high FIP elements remain unchanged, while all low FIP elements are enhanced by a factor 3-4. The depletions of He and Ne are lost. The quiet sun observations of Bryans et al. (2009) are best matched at the frequency of  $0.075 \text{ rad s}^{-1}$  and with the exception of K, the consistency between their measurements and the model is excellent at an initial wave amplitude of  $0.7 \text{ km s}^{-1}$ .

Figures 6 and 7 illustrate the ponderomotive acceleration and FIP fractionation within the chromosphere for the cases of frequencies  $0.06$ ,  $0.07$ ,  $0.085$  and  $0.105 \text{ rad s}^{-1}$ . At  $0.06 \text{ rad s}^{-1}$ , the ponderomotive acceleration is positive from about  $800 \text{ km}$  up, and has a “spike” at about  $2150 \text{ km}$ , with maximum close to  $10^6 \text{ cm s}^{-2}$ . Fractionation of Fe, Mg, and S is similar low down, but the fractionation hierarchy  $\text{Fe} > \text{Mg} > \text{S}$  is established in the range  $1500\text{-}2000 \text{ km}$ . For  $0.07 \text{ rad s}^{-1}$ , the ponderomotive acceleration has a similar, but slightly larger maximum at about  $2150 \text{ km}$ . In response to this Fe, Mg and S undergo a similar and small inverse FIP fractionation up to  $1500 \text{ km}$ , giving way to positive FIP higher up. The fractionation pattern  $\text{Fe} > \text{Mg} > \text{S}$  is even stronger here than for  $0.06 \text{ rad s}^{-1}$ , and is mainly occurring at the “spike” in the ponderomotive acceleration. In the last two cases, the ponderomotive force is stronger lower down in the chromospheric, and the “spike” at  $2150 \text{ km}$  becomes less pronounced. The slow mode wave amplitude is also stronger lower down. At  $0.105 \text{ rad s}^{-1}$ , all fractionation occurs by  $1600 \text{ km}$ , and the local maximum in the ponderomotive acceleration at  $2150 \text{ km}$  has no effect.

These fractionation patterns have simple qualitative explanations. First we display in Figure 8, the  $0.07 \text{ rad s}^{-1}$  case again to illustrate the relation of the fractionation to important features of the chromosphere. The left panels give the ponderomotive acceleration (bottom) and the density and temperature structure of the chromosphere (top). The “spike” in the

ponderomotive acceleration can be seen to stem from the steep density gradient beginning at an altitude of about 2100 km. The solid and dashed lines in the bottom plot show the ponderomotive acceleration with and without the energy loss to slow mode waves. In the regions where significant fractionation occurs, the slow mode wave do not affect the ponderomotive acceleration very much, and their main effect on the fractionation is through the additional longitudinal pressure they provide. The panels on the right hand side show the same fractionations as before (bottom), and on the top an expanded view of the ionization fraction of the elements C, S, Mg, and Fe.

With reference to equation 3, in regions where H is predominantly neutral, (below about 1500 km altitude)  $\nu_{s,i} \sim \nu_{s,n}$  and similar fractionation results for elements where  $\xi_s$  is reasonably close to unity. Where H is predominantly ionized,  $\nu_{s,i} \gg \nu_{s,n}$ , and small departures in  $\xi_s$  from unity can make a big difference to the fractionation. This is the reason why S fractionates similarly to Fe and Mg in the low chromosphere, but markedly less so in higher regions. This is also the reason why Mg fractionates less than Fe higher up. At an altitude of 2000 km, the charge state fractions of Fe, Mg, and S are 0.9995, 0.9981, and 0.9942 respectively (see Figure 8). Even though these are close to unity, the differences from unity result in different fractionations where the H ionization fraction (which closely follows that of O) is about 0.6. Lower down, where H is mostly neutral, the different ionization fractions matter much less in the fractionation. Recalling the results calculated using the Saha approximation for the ionization fractions, we can now see why Mg and Fe fractionate much more similarly in this case. The ionization fractions at 2000 km altitude are now 0.999974, 0.999995, and 0.9983 respectively, for Fe, Mg, and S. These are much closer to unity than before, so Fe and Mg now fractionate to a more similar degree. This is to be expected, since the assumption of LTE in the Saha equation suppresses radiative recombination rates, since the photons so produced cannot escape, and so the Saha ionization fractions will be higher than a more realistic calculation would predict.

However in Table 1 using Saha equilibrium, Fe and Mg do not behave exactly identically. Recalling equation 3,

$$\text{fractionation} = \exp \left( 2 \int_{z_l}^{z_u} \frac{\xi_s a \nu_{s,n}}{[\xi_s \nu_{s,n} + (1 - \xi_s) \nu_{s,i}]} \frac{1}{[kT/m_s + v_{\mu turb}^2 + v_{turb}^2]} dz \right) \quad (17)$$

and remembering that  $v_{turb}$  is the amplitude of slow mode waves generated by the Alfvén waves themselves, we can see that when  $v_{turb}$  and  $v_{\mu turb}$  dominate over the ion thermal speed (usually  $v_{turb} > v_{\mu turb}$ ), the mass dependence disappears from this part of the equation, and will only reside, if at all, in the collision frequencies. In fractionation occurring high in the chromosphere associated with the “spike”, where the plasma temperature is increasing rapidly up to coronal values, this condition may not be met and mass dependent fractiona-

tion can occur. In fractionation occurring lower down near the chromospheric temperature minimum, for example in the  $0.085 \text{ rad s}^{-1}$  case, this condition is met, and quasi-mass independent fractionation results.

## 5. Discussion

### 5.1. The Effect of Slow Mode Waves

The parametric generation of slow mode wave is a crucial part of the fractionation process by ponderomotive forces. One important effect has been to render the fractionation quasi mass independent as is often observed. This is demonstrated most clearly in Figure 7a, corresponding to a  $0.085 \text{ rad s}^{-1}$  Alfvén wave, the case which also has the highest slow mode wave amplitude, staying close to  $10 \text{ km s}^{-1}$  for large regions of the chromosphere where thermal speeds are  $\sim 1 \text{ km s}^{-1}$ . Fractionation occurring at the top of the chromosphere in the location of the “spike” in the ponderomotive acceleration often retains some mass dependence, because the plasma temperature is increasing rapidly here while the slow mode wave amplitude is usually small.

In the case that  $\delta v_s \sim \delta v_A$  as in Laming (2009), the increased slow mode wave amplitude relative to this work suppresses all FIP fractionation except when the wave frequency coincides precisely with the loop resonance, and then all fractionation occurs at the loop top and hence is mass dependent. For reasons we discuss below, this coincidence is probably not realized ubiquitously in the solar corona. Moreover the assumption of isotropic turbulence probably requires a well developed turbulent cascade, which is unlikely to develop with purely parallel propagating waves (e.g. Luo & Melrose 2006). Lower down in the chromosphere as the plasma beta approaches unity, the magnetic field becomes more concentrated in network segments. The increased curvature of field lines will lead initially parallel propagating waves to develop perpendicular components to their wavevectors, and hence turbulent cascade or mode conversion become more likely. Our equation 15 above is an attempt to capture this behavior, and obviously needs to be revisited with greater rigor.

### 5.2. The Alfvén Wave Frequency

Table 5 displays FIP fractionations for a range of frequencies close to the fundamental of a loop with length 100,000 km and magnetic field 20 G, with wave amplitudes chosen such that the fractionation of Fe/O is close to the usually observed value of 4. We commented above how the fractionation details of other elements vary slightly as the coronal wave moves

from being in coincidence with the loop resonance, to a position well off resonance. This arises because resonant waves reflect from the top of the chromosphere, and this is then the sole location of FIP fractionation, but nonresonant waves penetrate further down, allowing FIP fractionation to occur over a greater range of altitudes in the chromosphere.

When FIP fractionation is concentrated at the top of the chromosphere, the different ionization structures of the various high FIP elements becomes important, and fractionation occurs among them. Most significantly, He becomes depleted relative to O, with this depletion being strongest for a frequency  $0.075 \text{ rad s}^{-1}$ , just higher than the resonance, at a value of 0.60. This gives an abundance close to the He abundance frequently observed in the slow speed solar wind (Aellig et al. 2001; Kasper et al. 2007). In this frequency region too, C and possibly S also have minima in their fractionations. These elements have ionization potentials of 11.26 and 10.36 eV respectively (on the boundary between low FIP and high FIP elements). Although they are highly ionized throughout the chromosphere, as described above, they have sufficient neutral component that they fractionate well when H is predominantly neutral, but not when H is ionized. When fractionation is restricted to the top of the chromosphere where H is ionized, they behave more like high FIP elements. This is commonly seen in spectroscopic observations of S (e.g. Laming et al. 1995; Feldman et al. 2009; Widing & Feldman 2008; Brooks & Warren 2011).

Off resonance, when FIP fractionation can occur over a more extended range of heights, including those where H is mainly neutral, C and S might be expected to behave more like low FIP elements. Such behavior is more apparent in the solar wind observations of Zurbuchen et al. (2002) and von Steiger et al. (2000). Here, the FIP bias is variable, so that the time average over an extended period gives  $\text{Fe/O} \sim 2$  instead of  $\sim 4$  as modeled. Even so,  $\text{S/O}$  has a similar value to  $\text{Fe/O}$ . These observations are best matched in Table 5 for a frequency  $0.085 \text{ rad s}^{-1}$ .

We have previously suggested that Alfvén waves of coronal origin probably derive from coronal heating mechanisms such as nanoflares or Alfvén resonance. The coronal Alfvén amplitudes required above ( $\sim 50 - 100 \text{ km s}^{-1}$ ) are larger than nonthermal mass motions observed through spectral linewidths by factors 2-3. This suggests that the Alfvén wave must be confined to a small fraction of the loop cross-sectional area, which would also be a natural consequence of nanoflare or Alfvén resonance heating.

In as far as the heating can be considered a small perturbation to the coronal loop, the waves so generated should be eigenfunctions of the loop, with frequencies constrained to coincide with the loop resonance(s). The fact that many observations are better matched by Alfvén wave frequencies slightly higher than the resonance possibly suggests a dynamic system. The loop releases waves at its resonance as part of the heating process. The heat

conducts down to the chromosphere, and heated plasma there evaporates back upwards into the loop (e.g. Patsourakos & Klimchuk 2006), thus increasing its density and reducing the coronal Alfvén speed, and hence also reducing the loop resonance frequency. The waves produced at the original resonance continue to propagate until damped. So we might naturally expect a mismatch between Alfvén wave frequency and the loop resonance, and also expect this mismatch to become larger in more strongly heated region of the corona, e.g. active region and flares, as opposed to quiet sun. Of course this discussion presupposes that the heating is a weak perturbation to the coronal loop, and so its eigenfunctions are well defined, and can be excited. In flares and CMEs, this might no longer be true, and the heating mechanism itself will determine which waves are produced, irrespective of the loop boundary conditions.

Such ideas will be investigated in greater detail in a separate paper. For the time being, we restrict ourselves to some simple predictions. The coronal helium abundance should increase with increasing solar activity, as it appears to do both in solar wind observations (Aellig et al. 2001; Kasper et al. 2007) and in spectroscopic measurements of the quiet sun (Laming & Feldman 2001, 2003) compared to flares (Feldman et al. 2005). The S and C abundance should also vary. In the solar wind (e.g. von Steiger et al. 2000) it appears to vary as a low FIP ion, whereas in spectroscopic observations, (e.g. Laming et al. 1995; Feldman et al. 2009, of quiet and active regions) sulfur is observed to behave as a high FIP element.

### 5.3. The Upward Flow Speed

We have suggested conduction driven chromospheric evaporation as the source of the plasma upflow that populates the corona with fractionated gas. Here we estimate the flow speed in the chromosphere, and show that it is consistent with limits set by the operation of the ponderomotive force producing the FIP fractionation. With  $d\rho/dt = 0$  we write

$$\frac{\partial}{\partial z}(\rho v) = -\frac{\partial \rho}{\partial t} = -\frac{\mu g z}{k_B T^2} \frac{\partial T}{\partial t} \rho \quad (18)$$

where the density  $\rho \propto \exp(-\mu g z/k_B T)$  is a gravitationally stratified solution. The mean molecular mass is  $\mu$ , and  $k_B$  is Boltzmann’s constant. Integrating between  $z_l$  and  $z_u$

$$\rho(z_u) v(z_u) - \rho(z_l) v(z_l) = - \int_{z_l}^{z_u} \frac{\mu g z}{k_B T^2} \frac{\partial T}{\partial t} \rho dz. \quad (19)$$

We choose the upper limit  $z_u$  to be where  $v(z_u) = 0$  in the corona, and so

$$v(z_l) = \int_{z_l}^{z_u} \frac{z}{L_\rho} \frac{\rho(z)}{\rho(z_l)} \frac{\partial \ln T}{\partial t} dz = \int_{z_l}^{z_u} \frac{z}{L_\rho} \exp\left(-\frac{z}{L_\rho}\right) \frac{\partial \ln T}{\partial t} dz \quad (20)$$



where  $L_\rho = k_B T / \mu g$  is the density scale height. This integral will be dominated by the integrand near  $z = z_l$ , so

$$v(z_l) \simeq L_\rho \frac{\partial \ln T}{\partial t} \simeq \frac{2L_\rho}{5nk_B T} \frac{\partial}{\partial z} \left( 10^{-6} T^{5/2} \frac{\partial T}{\partial z} \right) \sim 10^{17} \frac{T^{1/2}}{n} \left( \frac{\Delta T}{L_T} \right)^2 \quad (21)$$

where we have put  $2.5nk_B \partial T / \partial t = -\nabla \cdot \mathbf{Q}$  with the heat flux  $\mathbf{Q} = -10^{-6} T^{5/2} \nabla T$ . The temperature gradient has been replaced by  $\Delta T / L_T$ , where  $\Delta T$  may be the coronal peak temperature, and  $L_T$  the loop half-length. Taking the chromospheric temperature  $T \sim 10^4$ ,

$$v(z_l) \simeq \frac{10^{13}}{n} \left( \frac{T_c / 5 \times 10^6 \text{ K}}{L_T / 5 \times 10^9 \text{ cm}} \right)^2 \text{ cm s}^{-1}, \quad (22)$$

which suggests a velocity of  $10^3 \text{ cm s}^{-1}$  at a density of  $10^{10} \text{ cm}^{-3}$ . This may well be an underestimate due to our approximation for the temperature gradient, but as discussed in Laming (2004), is sufficiently high that gravitational settling should not occur. If  $v(z_l)$  approaches  $\sim 1 \text{ km s}^{-1}$ , as might happen in flares, some further discussion is required.

The derivation of equation 17 neglected inertial terms in the momentum equations for ions and neutrals. Reinstating these, in the limit that  $u_{si} - u_{sn} \ll u_s \sim u$  the fractionation becomes

$$\text{fractionation} = \exp \left( 2 \int_{z_l}^{z_u} \frac{\xi_s a \nu_{s,n}}{[\xi_s \nu_{s,n} + (1 - \xi_s) \nu_{s,i}]} \frac{1}{[kT/m_s + v_{\mu turb}^2 + v_{turb}^2 + u_{flow}^2]} dz \right). \quad (23)$$

When the magnitude of  $u_{flow}^2$  approaches those of the other terms in the second square bracket in the denominator of the integrand, some reduction in the FIP effect will result. This is most likely to have an impact on fractionation occurring at the top of the chromosphere, taking  $\rho u_{flow} \sim \text{constant}$  through the chromosphere, and will possibly reduce the amount of mass dependent fractionation occurring there. This will happen for relatively large flow speeds  $u_{flow} \sim 1 \text{ km s}^{-1}$  or larger at the top of the chromosphere, still significantly lower than the Alfvén speed in this region.

## 5.4. Conclusions

We have further developed the model of element fractionation to give rise to the FIP effect by the ponderomotive force, paying careful attention to the generation of slow mode waves by the primary Alfvén oscillations. When considering a realistic wave spectrum with both chromospheric and coronal contributions, the extra longitudinal pressure due to the slow mode waves is crucial in producing the correct fractionation. With this extra

ingredient, together with the improvements to the ionization balance and the normalization of the fractionation, a rather comprehensive description of the coronal fractionation has emerged. In seeking to understand the FIP effect as usually described, we have also found an explanation for the depletion of He in the solar wind, and also possibly its variation. The Ne abundance also appears to vary in a similar manner, but to a lesser degree. It is also more sensitive to assumptions about the ionization balance, but further investigation of this is expected to resolve current controversy surrounding the solar photospheric abundance of this element.

The theory now appears to be developed to the point where variations in the FIP fractionation from place to place in the solar corona or wind may now be interpreted in terms of their physical origins. The element abundances in the solar corona may therefore be considered as diagnostics of the behavior of MHD turbulence, and also thereby of the mechanisms that heat the solar corona. These ideas will be further developed in subsequent papers.

This work was supported by NASA Contracts NNN10A055I, NNN11AQ23I, and by basic research funds of the Office of Naval Research. I am also grateful to Cara Rakowski for a critical reading of an earlier draft of this paper.

## REFERENCES

- Aellig, M. R., Lazarus, A. J., & Steinberg, J. T. 2001, *GRL*, 28, 2767
- Allan, R. J., Clegg, R. E. S., Dickinson, A. S., & Flower, D. R. 1988, *MNRAS*, 235, 1245
- Avrett, E., & Loeser, R. 2008, *ApJS*, 175, 229
- Banaskiewicz, M., Axford, W. I., & McKenzie, J. F. 1998, *A&A*, 337, 940
- Brooks, D. H., & Warren, H. P. 2011, *ApJ*, 727, L13
- Bryans, P., Landi, E., & Savin, D. W. 2009, *ApJ*, 691, 1540
- Cally, P. S., & Goossens, M. 2008, *Sol. Phys.*, 251, 251
- Carlsson, M., & Stein, R. F. 2002, *ApJ*, 572, 626
- Cranmer, S. R. 2009, *Living Reviews of Solar Physics*, 6, 3
- Cranmer, S. R., van Ballegooijen, A. A., & Edgar, R. J. 2007, *ApJS*, 171, 520

- Cranmer, S. R., & van Ballegooijen, A. A. 2005, *ApJS*, 156, 265
- Del Zanna, L., Schaekens, E., & Velli, M. 2005, *A&A*, 431, 1095
- Feldman, U., Landi, E., & Laming, J. M. 2005, *ApJ*, 619, 1142
- Feldman, U., Warren, H. P., Brown, C. M., & Doschek, G. A. 2009, *ApJ*, 695, 36
- Ferland, G. J., Korista, K. T., Verner, D. A., & Dalgarno, A. 1997, *ApJ*, 481, L115
- Giammanco, C., Wurz, P., & Karrer, R. 2008, *ApJ*, 681, 1703
- Giammanco, C., Wurz, P., Opitz, A., Ipavich, F. M., & Paquette, J. A. 2007, *AJ*, 134, 2451
- Hollweg, J. V. 1984, *ApJ*, 277, 392
- Huba, J. D., Warren, H.P., Joyce, G., Pi, X., Iijima, B., & Coker, C. 2005, *GRL*, 32, L15103
- Kasper, J. C., Stevens, M. L., Lazarus, A. J., Steinberg, J. T., & Ogilive, K. W. 2007, *ApJ*, 660, 901
- Khomenko, E., & Cally, P. S. 2011, *J. Phys. Conf. Ser.* 271, 012042
- Khomenko, E. 2010, in *Highlights of Spanish Astrophysics V, Astrophysics and Space Science Proceedings*, (Spring-Verlag: Berlin Heidelberg), p 51
- Kingdon, J. B., & Ferland, G. J. 1996, *ApJS*, 106, 205
- Ko, Y.-K., Raymond, J. C., Zurbuchen, T. H., Riley, P., Rainers, J. M., & Strachan, L. 2006, *ApJ*, 646, 1275
- Laming, J. M., & Feldman, U. 2001, *ApJ*, 546, 552
- Laming, J. M., & Feldman, U. 2003, *ApJ*, 591, 1257
- Laming, J. M. 2004, *ApJ*, 614, 1063
- Laming, J. M., Drake, J. J., & Widing, K. G. 1995, *ApJ*, 443, 416
- Laming, J. M. 2009, *ApJ*, 695, 954
- Landau, L. D., & Lifshitz, E. M. 1976, *Mechanics*, (Oxford: Pergamon Press)
- Luo, Q., & Melrose, D. 2006, *MNRAS*, 368, 1151
- McKenzie, D. L., & Feldman, U. 1994, *ApJ*, 420, 892

- Patsourakos, S., & Klimchuk, J. A. 2006, *ApJ*, 647, 1452
- Phillips, K. J. H., Sylwester, J., Sylewester, B., & Landi, E. 2003, *ApJ*, 589, L113
- Phillips, K. J. H., Aggarwal, K. M., Landi, E., & Keenan, F. P. 2010, *A&A*, 518, A41
- Schwadron, N. A., Fisk, L. A., & Zurbuchen, T. H. 1999, *ApJ*, 521, 859
- Sylwester, J., Sylwester, B., Phillips, K. J. H., & Kuznetsov, V. D. 2010, *ApJ*, 710, 804
- Sylwester, J., Sylwester, B., Phillips, K. J. H., & Kuznetsov, V. D. 2010, *ApJ*, 720, 1721
- Vasheghani Farahani, S., Nakariakov, V. M., Van Doorselaere, T., & Verwichte, E. 2011, *A&A*, 526, A80
- Vernazza, J., & Reeves, E. M. 1978, *ApJS*, 37, 485
- Vernazza, J., Avrett, E. H., & Loeser, R. 1981, *ApJS*, 45, 635
- von Steiger, R., Schwadron, N. A., Fisk, L. A., Geiss, J., Gloeckler, G., Hefti, S., Wilken, B., Wimmer-Schweingruber, R. F., & Zurbuchen, T. H. 2000, *JGR*, 105, 27217
- Wedemeyer-Böhm, S., & Carlsson, M. 2011, *A&A*, 528, 1
- Widing, K. G., & Feldman, U. 2008, *ApJ*, 675, 863
- Wood, B. E., & Linsky, J. L. 2010, *ApJ*, 717, 1279
- Zaqarashvili, T. V., & Roberts, B. 2006, *A&A*, 452, 1053
- Zurbuchen, T. H., Fisk, L. A., Gloeckler, G., & von Steiger, R. 2002, *Geophys. Res. Lett.* 29, 1352

Table 1: FIP Fractionations in Different Approximations

ratio	baseline <sup>a</sup>	density mod. <sup>b</sup>	Saha ionization <sup>c</sup>	$\delta v_z = \delta V_A$
He/O	0.67	0.83	0.73	0.85
C/O	0.99	1.26	1.17	1.03
N/O	0.82	1.02	0.95	0.93
Ne/O	0.74	0.93	0.90	0.89
Mg/O	1.98	2.52	2.33	1.43
Si/O	1.89	2.37	2.41	1.41
S/O	1.40	1.75	1.47	1.23
Ar/O	0.92	1.16	1.03	0.97
Fe/O	3.29	4.17	2.79	1.87

---

Note. — <sup>a</sup> Baseline model corresponds to a coronal peak Alfvén wave amplitude of  $\sim 60 \text{ km s}^{-1}$ , and the standard chromospheric model. <sup>b</sup> gives results with chromosphere density modified to be consistent with photoionization-recombination equilibrium and the temperature in the Avrett & Loeser (2008) model. <sup>c</sup> give results with the ionization fraction for each element modified to be given by Saha equilibrium at the temperature and density given by Avrett & Loeser (2008). The final column shows the effect of the approximation of Laming (2009), where isotropic turbulence is assumed.

Table 2: Open Magnetic Field Wave Spectra at 500,000 km Altitude

ang. freq.	v0	v1	v2
0.010	12.5	12.5	125
0.031	150	150	150
0.062	75	75	75
0.093	50	50	50
0.124	12.5	125	12.5

---

Note. — Frequencies are angular frequencies in  $\text{rad s}^{-1}$ . Velocities are in  $\text{km s}^{-1}$ ; v0 is designed to match Fig. 3 in Cranmer et al. (2007).

Table 3: FIP Fractionations in Open Magnetic Field

ratio	models			observations		
	v0	v1	v2	a	b	c
He/O	0.90	0.85	0.85	0.60-0.58	0.37-0.47	0.45-0.55
C/O	1.13	1.18	1.10	1.50-1.41	1.17-1.35	0.9 - 1.1
N/O	0.96	0.94	0.94	1.19-0.9	0.64-0.99	
Ne/O	0.95	0.92	0.92	0.48-0.47	0.40-0.56	0.3 - 0.4
Na/O	1.97	2.99	2.04			
Mg/O	1.65	2.21	1.67	1.73-1.92	0.98-1.60	0.95 - 2.45
Al/O	1.72	2.37	1.75			
Si/O	1.51	1.89	1.53	2.07-1.92	1.20-2.09	0.9 - 1.8
S/O	1.26	1.39	1.26	1.53-1.56	1.38-2.57	
Ar/O	1.00	0.99	0.99			
K/O	2.03	3.14	2.12			
Ca/O	1.88	2.74	1.93			
Fe/O	1.97	2.97	2.04	1.42-1.73	1.04-1.69	0.65 - 1.35
Ni/O	1.85	2.67	1.91			
Kr/O	1.01	1.01	1.01			
Rb/O	1.97	2.94	2.04			
W/O	1.99	2.99	2.07			

---

Note. — From left to right, model FIP fractionations correspond to the chromospheric model in Fig. 3. Observational ratios are taken from, (a) Zurbuchen et al. (2002), (b) von Steiger et al. (2000), (c) Ko et al. (2006), all given relative to O. Ranges quoted from von Steiger et al. (2000) include their uncertainties.

Table 4: FIP Fractionations in Closed Magnetic Field I

ratio	models			observations					
	0.4	0.5	0.6	a	b	c	d	e	f
	(km s <sup>-1</sup> )								
He/O	0.72	0.61	0.47	0.68-0.60	0.29-0.75				
C/O	1.01	1.03	0.97	1.36-1.41	1.06-1.37				
N/O	0.86	0.81	0.69	0.72-1.32	0.22-0.89				
Ne/O	0.86	0.71	0.57	0.58	0.38-0.75				
Na/O	2.42	3.96	6.74			7.8 <sup>+13</sup> <sub>-5</sub>	1.8 <sup>+2</sup> <sub>-1</sub>		
Mg/O	1.76	2.35	3.25	2.58-2.61	1.08-2.36	2.8 <sup>+2.3</sup> <sub>-1.3</sub>	2.7±0.3		
Al/O	1.95	2.82	4.12			3.6 <sup>+1.7</sup> <sub>-1.2</sub>	5.6 <sup>+3.3</sup> <sub>-2.1</sub>		
Si/O	1.70	2.27	3.02	2.49-3.11	1.36-3.24	4.9 <sup>+2.9</sup> <sub>-1.8</sub>			
S/O	1.34	1.57	1.78	1.62-1.92	1.23-2.68	2.2±0.2	2.1±0.2	1.7 ± 0.3	
Ar/O	0.96	0.94	0.86					1.1 ± 0.1	1.12±0.15
K/O	2.72	4.70	8.51			1.8 <sup>+0.4</sup> <sub>-0.6</sub>	4.7 <sup>+7.0</sup> <sub>-2.8</sub>	3.5 ± 0.9	6
Ca/O	2.38	3.80	6.27			3.5 <sup>+4.3</sup> <sub>-1.9</sub>	2.7±0.25		3.0-9.7
Fe/O	2.65	4.44	7.85	2.28-2.90	0.96-2.46	7.0 <sup>+1.4</sup> <sub>-1.2</sub>			
Ni/O	2.59	4.10	6.92						
Kr/O	0.99	1.00	0.92						
Rb/O	2.84	4.96	9.01						
W/O	3.01	5.35	9.85						

Note. — From left to right, model FIP fractionations correspond to the chromospheric model in Fig. 3. The models for 0.4, 0.5 and 0.6 km s<sup>-1</sup> refer to the amplitude with which the coronal wave is initiated in the low chromosphere. The corresponding coronal wave amplitudes are 55, 67, and 82 km s<sup>-1</sup> respectively. Observational ratios are taken from, (a) Zurbuchen et al. (2002), given relative to O, (b) von Steiger et al. (2000), relative to O, (c) Bryans et al. (2009), given relative to the mean of O, Ne and Ar, (d) Giammanco et al. (2007, 2008), relative to H, and (e) Phillips et al. (2003), relative to H, (f) Sylwester et al. (2010ab) and McKenzie & Feldman (1994), relative to H, all given relative to the photospheric abundance of Grevesse & Sauval (1998). Ranges quoted from von Steiger et al. (2000) include their uncertainties.

Table 5: FIP Fractionations in Closed Magnetic Field II

ang. freq. (rad s <sup>-1</sup> )	0.055	0.06	0.065	0.07	0.075	0.08	0.085	0.09	0.105
$v_{init}$ (km s <sup>-1</sup> )	0.255	0.25	0.35	0.45	0.55	0.5	0.45	0.36	0.193
$v_{cor}$ (km s <sup>-1</sup> )	40	40	45	60	70	60	50	38	20
ratio									
He/O	0.84	0.81	0.74	0.63	0.60	0.74	0.86	0.94	0.98
C/O	1.43	1.38	1.32	1.18	1.23	1.40	1.53	1.59	1.56
N/O	0.93	0.92	0.89	0.83	0.80	0.88	0.94	0.97	0.99
Ne/O	0.90	0.89	0.84	0.75	0.72	0.83	0.91	0.96	0.98
Na/O	4.74	4.47	4.61	4.31	4.47	4.36	4.69	4.73	4.60
Mg/O	3.29	3.13	3.11	2.74	2.89	3.13	3.49	3.59	3.51
Al/O	3.59	3.43	3.49	3.15	3.30	3.42	3.73	3.81	3.75
Si/O	2.70	2.63	2.69	2.51	2.69	2.74	2.88	2.89	2.84
S/O	1.79	1.77	1.79	1.72	1.83	1.86	1.92	1.90	1.87
Ar/O	0.98	0.98	0.97	0.96	0.94	0.97	0.99	0.99	1.00
K/O	5.08	4.85	5.13	4.84	4.92	4.68	4.95	4.98	4.94
Ca/O	4.31	4.13	4.32	4.00	4.12	4.06	4.34	4.39	4.36
Fe/O	4.78	4.60	4.87	4.52	4.57	4.44	4.73	4.79	4.79
Ni/O	4.20	4.09	4.35	4.12	4.23	4.06	4.24	4.25	4.27
Kr/O	1.00	1.00	1.00	1.00	0.99	1.00	1.00	1.00	1.00
Rb/O	4.73	4.61	4.98	4.79	4.80	4.50	4.67	4.67	4.72
W/O	4.84	4.73	5.15	4.83	4.83	4.56	4.76	4.79	4.89

---

Note. — Entries in rows  $v_{init}$  and  $v_{cor}$  refer to the amplitude with which the coronal wave is initiated in the low chromosphere, and it corresponding amplitude in the corona.



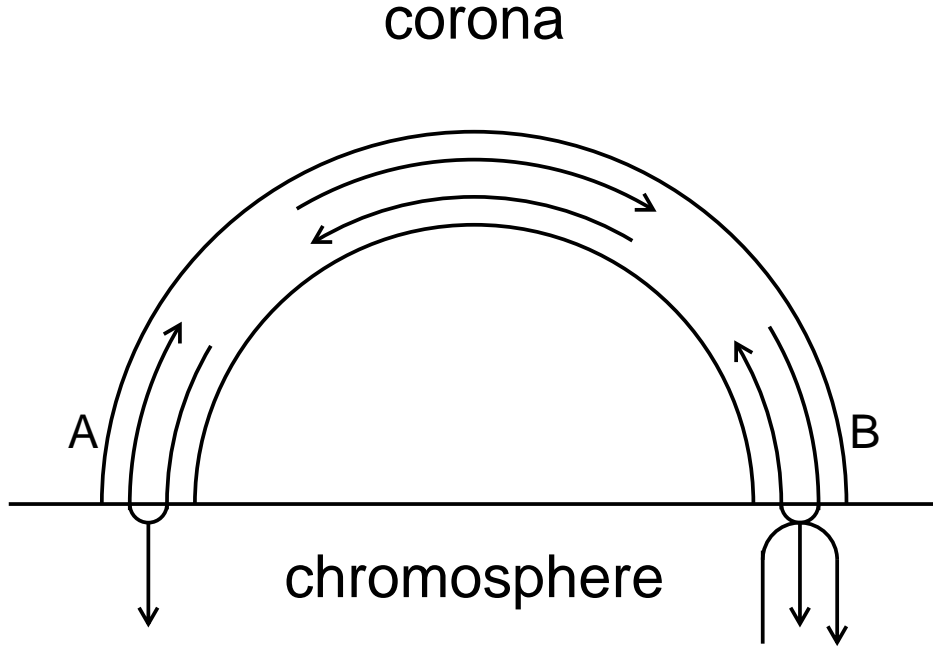


Fig. 1.— Cartoon illustrating the model. Alfvén waves generated in the corona either reflect from each footpoint or precipitate down, depending on their frequency with respect to the loop resonance. Resonant waves reflect, nonresonant waves precipitate down. Upcoming waves in the chromosphere, deriving from the mode or parametric conversion of p-modes at the  $\beta = 1.2$  layer, are generally reflected back downwards, as illustrated at footpoint B. In our models, we specify wave amplitudes at footpoint A, and integrate the non-WKB transport equation back to footpoint B, where FIP fractionations are evaluated.

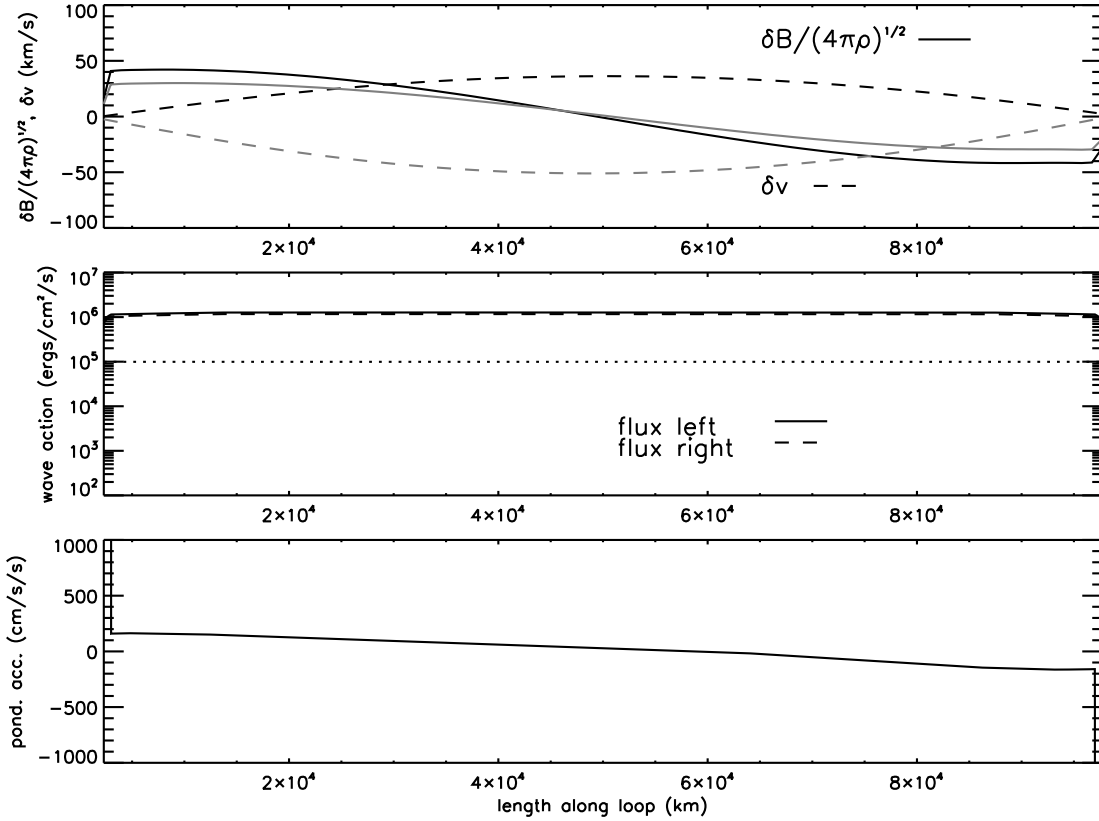


Fig. 2.— Coronal section of loop, length 100,000 km, magnetic field 20 G, (half wavelength long for a  $0.07 \text{ rad s}^{-1}$  angular frequency Alfvén wave) showing from top: Elsässer variables in  $\text{km s}^{-1}$  ( $\delta B/\sqrt{4\pi\rho}$  solid lines,  $\delta v$  dashed lines), with black lines for real parts and gray lines for imaginary parts. Middle; wave energy fluxes in  $\text{ergs cm}^{-2} \text{ s}^{-1}$ , the thin solid line shows the difference in energy fluxes divided by the magnetic field strength and should be a horizontal line if energy is properly conserved. Bottom, the ponderomotive acceleration in  $\text{cm s}^{-2}$ . Positive acceleration means positive along the  $z$  axis, which is upwards pointing near  $z = 0$  and downwards near  $z = 100,000$ .

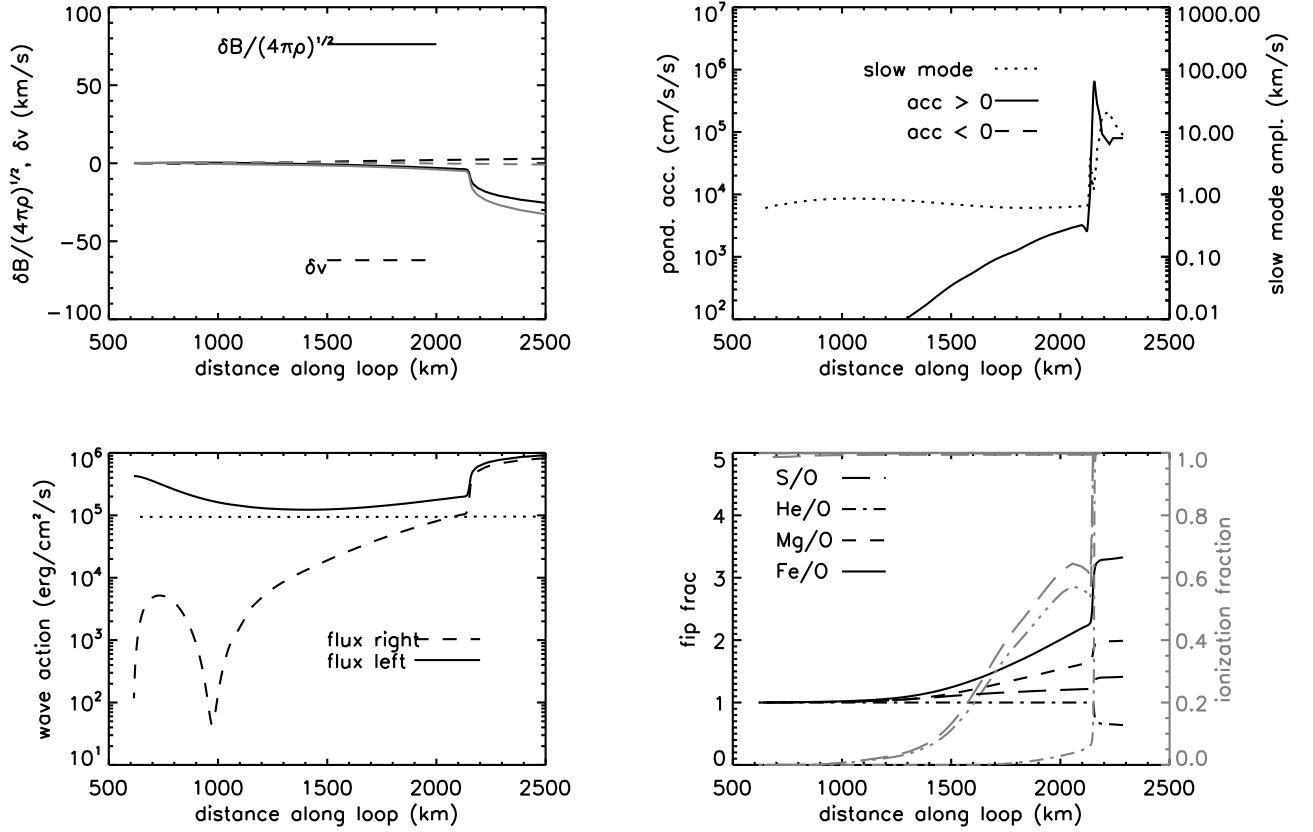


Fig. 3.— Same as figure 2 giving the first three panels for the left hand chromosphere “B”, where waves leak down from the corona. The extra bottom right panel shows the FIP fractionations (in black) for the ratios Fe/O, Mg/O, S/O and He/O. Chromospheric ionization fractions are also shown in the fourth panel (in gray, to be read on the left hand axis) in the same linestyles as for the fractionation. The extra dash-triple dot gives the O ionization fraction, the long dash curve gives the H ionization fraction. Fe and Mg are essentially fully ionized throughout the fractionation region.

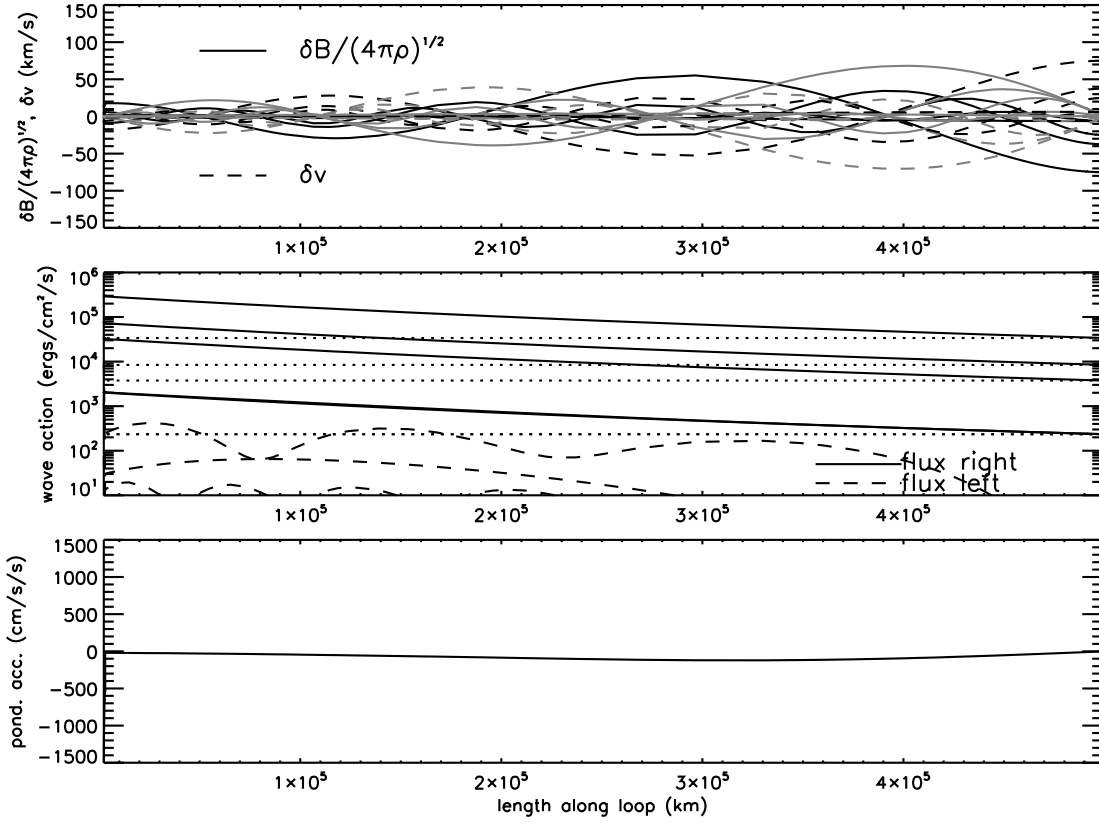


Fig. 4.— Same as figure 2 for an open field region. Five waves corresponding to the baseline model in Table 2 are considered, initiated at 500,000 km altitude and integrated back to the chromosphere.

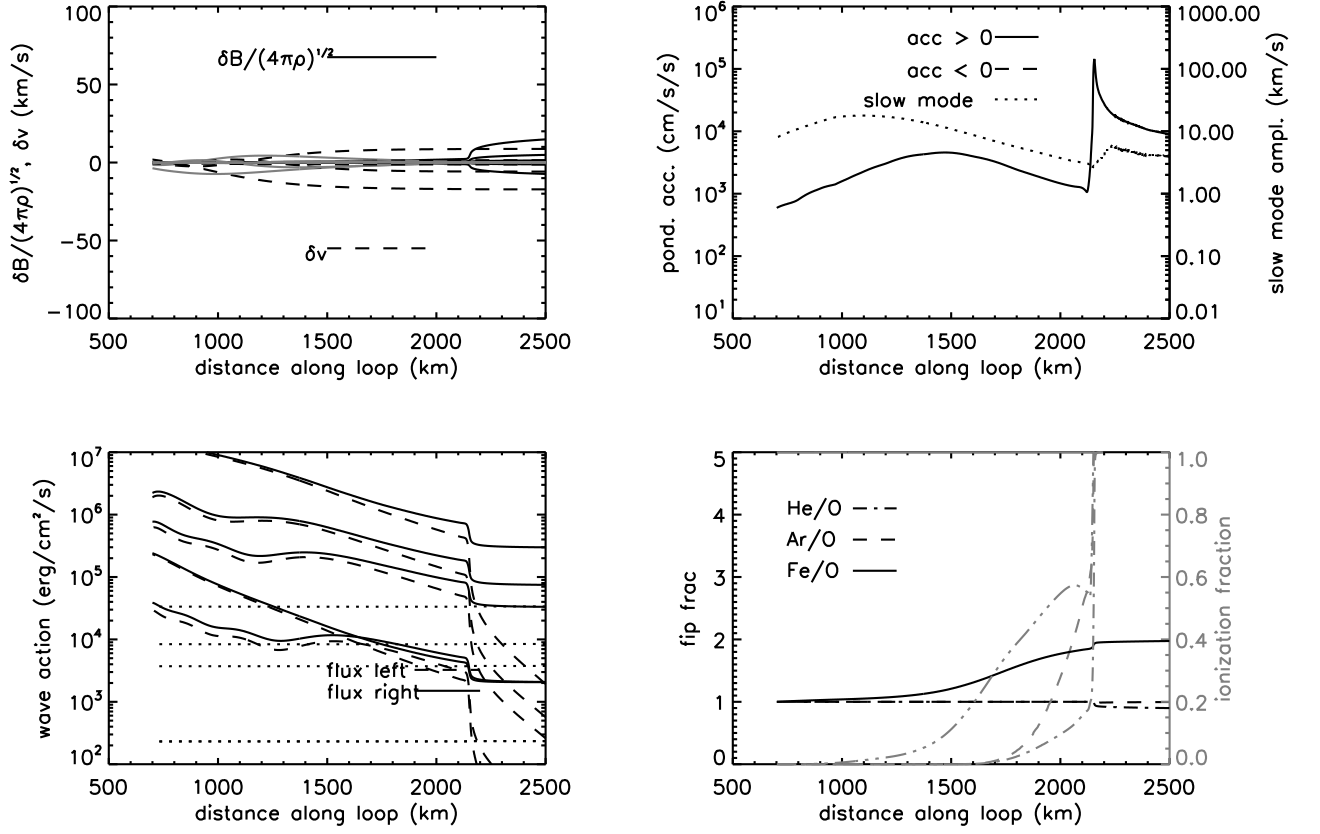


Fig. 5.— Chromospheric section of open field calculation of Figure 4. Fractionations are shown for Fe/O, Ar/O and He/O.

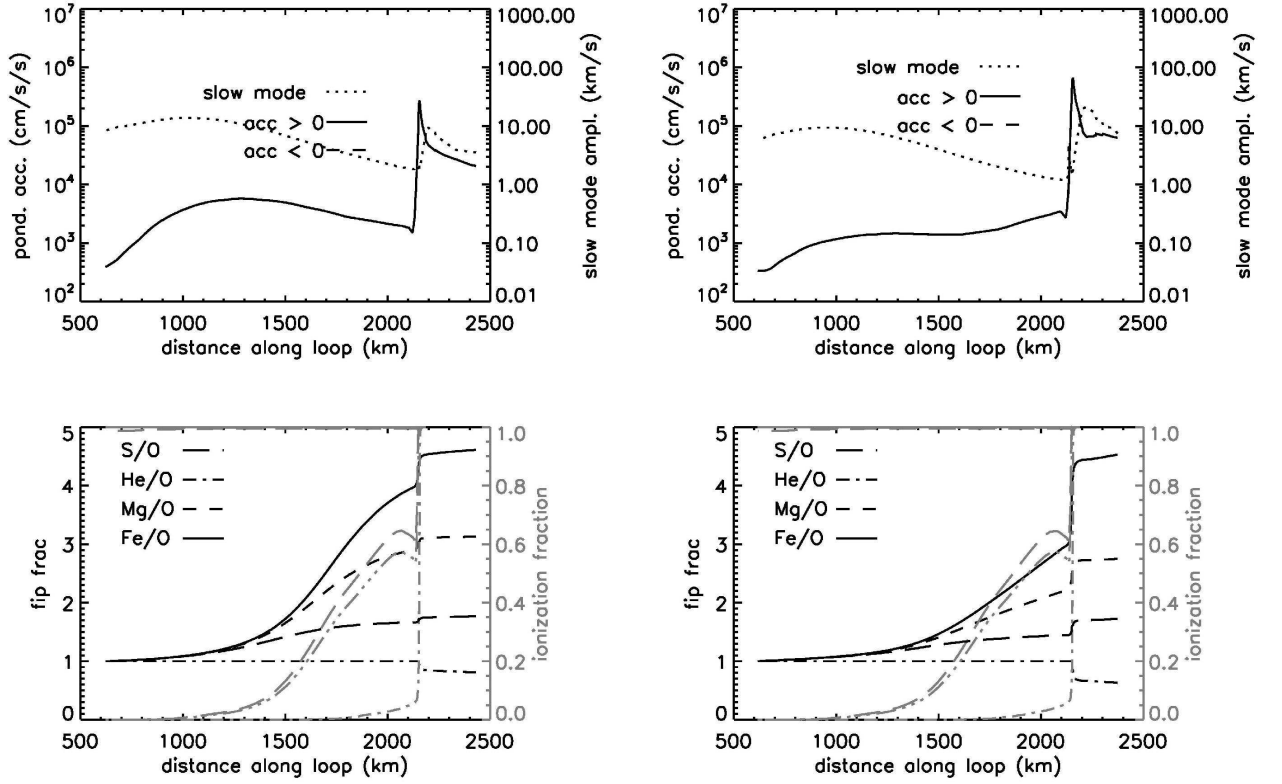


Fig. 6.— Ponderomotive force (top panels) and FIP fractionations (bottom panels) for the chromosphere including five chromospheric waves and a coronal wave with angular frequency 0.06 (left) and 0.07  $\text{rad s}^{-1}$  (right) respectively. Fractionations for Fe/O, Mg/O, S/O, and He/O are shown.

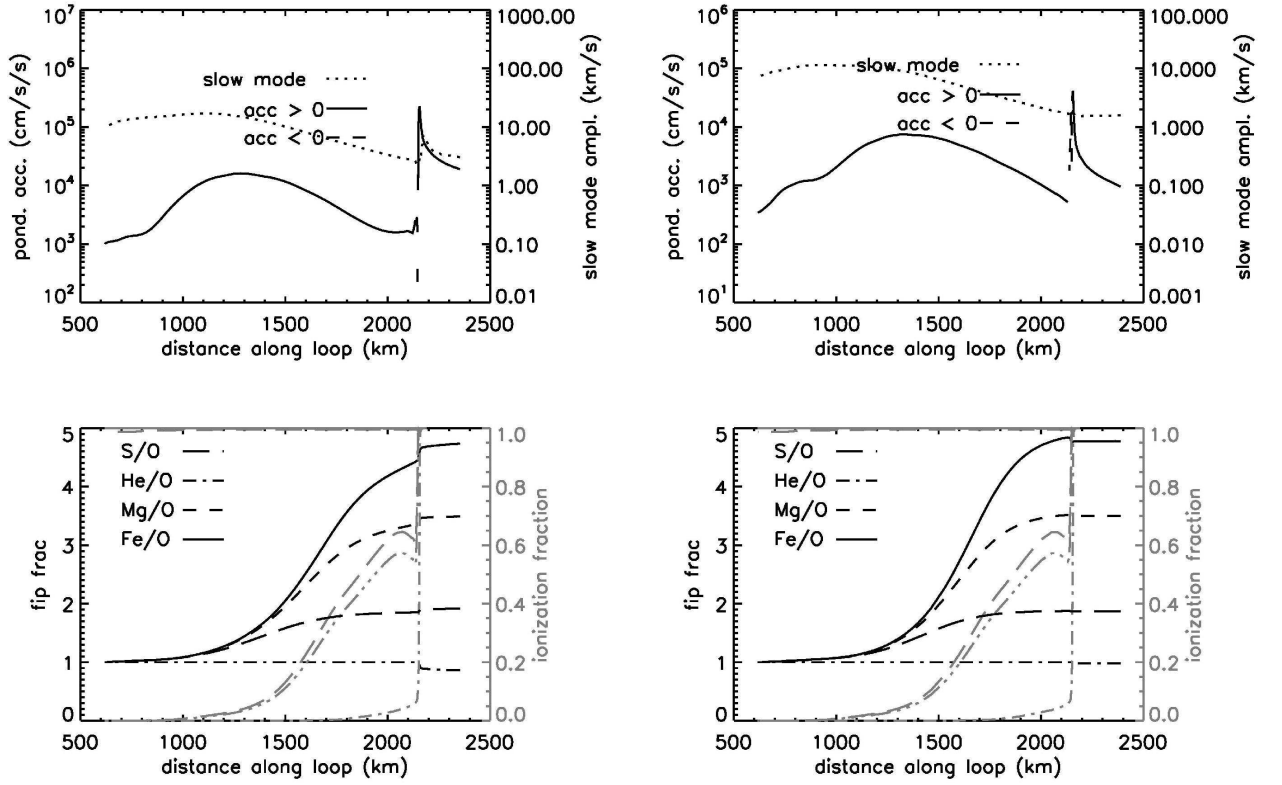


Fig. 7.— Ponderomotive force (top panels) and FIP fractionations (bottom panels) for the chromosphere including five chromospheric waves and a coronal wave with angular frequency 0.085 (left) and 0.0105 rad s<sup>-1</sup> (right) respectively. Fractionations for Fe/O, Mg/O, S/O, and He/O are shown. The 0.085 coronal wave gives a more similar FIP effect for Fe/O and Mg/O, as frequently observed. The He/O depletion reduces as the coronal wave moves off resonance, as the “spike” in the ponderomotive acceleration decreases in prominence.

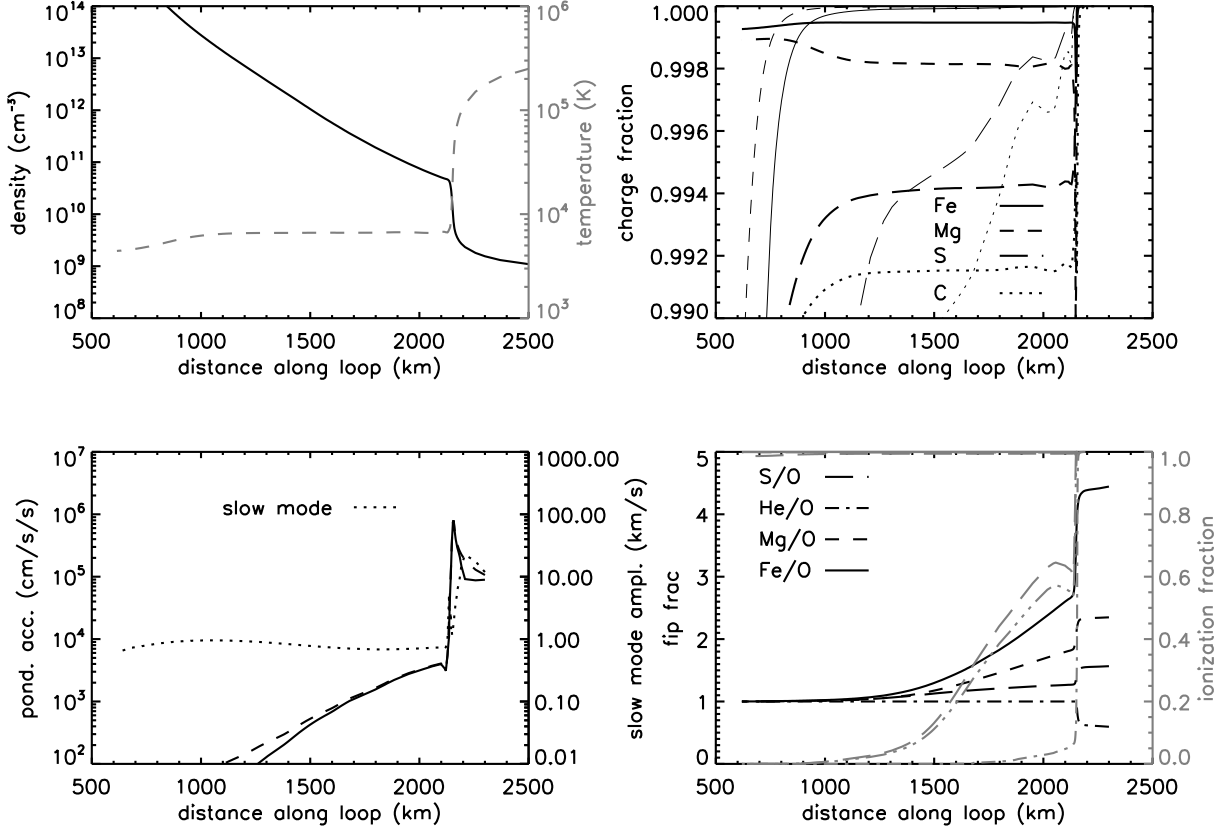


Fig. 8.— Illustration of FIP fractionation for the  $0.07 \text{ rad s}^{-1}$  wave, showing the correspondence with important features of the chromosphere. Top left gives the chromospheric density and temperature with height. Bottom left gives the ponderomotive acceleration as before, with solid and dashed curves showing the acceleration with and without energy loss to slow mode waves. The dotted curve shows the slow mode wave amplitude. The left panels show the “spike” in the ponderomotive acceleration at the altitude where the chromospheric density gradient is strongest. Bottom right is the same as before, with FIP fractionations for Fe/O, Mg/O, He/O, and S/O, together with ionization fractions. Top right shows the ionization fractions for C, S, Mg, and Fe in an expanded view. Thick curves correspond to the “baseline” charge state fractions used for FIP fractionation throughout this paper, thin curves give the results of the Saha approximation. This overestimates ionization fraction close to the top of the chromosphere, because photons resulting from radiative recombinations are not allowed to escape, but remain trapped to cause further photoionization.